Effect of External Magnetic Field on Hybrid Supercapacitors of Nitrogen-Doped Graphene with Magnetic Metal Oxides

Misganu Chewaka Fite, Jhan-Ying Rao, and Toyoko Imae*

The electrochemical analysis has shown the high capacitance performance of the nitrogen-doped graphene (NG) electrode, the capacitance increased by the in situ hybridization of NG with magnetic metal oxides, especially, with Fe_3O_4, and the further increase of the capacitance was brought by the application of the external magnetic field of 8.98 mT to be 1254 F/g at 5 mV/s.

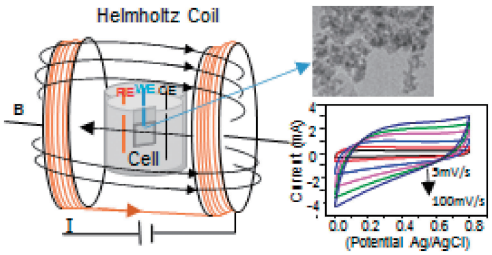

REPRINTED FROM

BCSJ Bulletin of the Chemical Society of Japan

Vol.93 No.9 2020 p.1139–1149

September 15, 2020

The Chemical Society of Japan

BCSJ

Document type: Article

Effect of External Magnetic Field on Hybrid Supercapacitors of Nitrogen-Doped Graphene with Magnetic Metal Oxides

Misganu Chewaka Fite,[1] Jhan-Ying Rao,[2] and Toyoko Imae*[1,2,3]

[1]Graduate Institute of Applied Science and Technology, National Taiwan University of Science and Technology, Taipei 10607, Taiwan

[2]Department of Chemical Engineering, National Taiwan University of Science and Technology, Taipei 10607, Taiwan

[3]Department of Materials Sciences and Engineering, National Taiwan University of Science and Technology, Taipei 10607, Taiwan

E-mail: imae@mail.ntust.edu.tw

Received: April 21, 2020; Accepted: May 14, 2020; Web Released: May 22, 2020

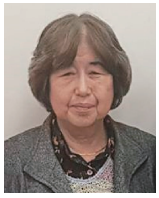

Toyoko Imae

Toyoko Imae received Doctor of Science degree from Nagoya University. She joined the National Taiwan University of Science and Technology, Taiwan, as an honorary chair professor in April 2009, immediately after retiring from Keio University, Japan. She has also been professor emeritus of Nagoya University, Japan, since 2006. Her major research areas are the fabrication, functionalization, and physicochemical investigation of nanomaterials, including polymers, nanoparticles, carbon materials, minerals and their composites. Her recent research target is "Nanoarchitecture and Nanotechnology" towards energy, environmental and biomedical sciences.

Abstract

In this report, nitrogen-, boron- and boron/nitrogen-doped graphene and nitrogen-doped carbon nanohorn were prepared. Electrochemical analysis has shown the higher capacitance performance of the nitrogen-doped graphene (NG) electrode, because nitrogen provides free valence electron to interact with electrolyte. Then magnetic metal oxides were in situ hybridized to a nitrogen-doped graphene to produce magnetic metal oxide/NG hybrid materials, and the electrochemical measurements of the prepared hybrid material electrodes were conducted without and with the external magnetic field (8.98 mT at the inflection point) of using a Helmholtz coil. The specific capacitance took an increasing order of NiO/NG (697 F/g, 747 F/g) < Co_3O_4/NG (963 F/g, 1092 F/g) < Fe_3O_4/NG (973 F/g, 1254 F/g) in an external magnetic field of (0 mT, 8.98 mT) at a scan rate of 5 mV/s. Although these electrodes displayed high capacitance and better charge/discharge profile, cycle retention (83 to 92% under no magnetic field) was not necessarily good or it fluctuated under 8.98 mT. These behaviours by the addition of magnetic metal oxides and external magnetic field are due to the electrical conductivity of metal oxides and the Lorentz force effect of the magnetic field, respectively. Thus, it can be confirmed that Fe_3O_4/NG hybrid has higher potential as a magnetic material electrode for supercapacitors and the magnetic field enhances the capacitance.

Keywords: External magnetic field | Hybrid supercapacitor | Magnetic metal oxide

1. Introduction

In recent years, human habitation has been reliably changing from a biofuel-dependent life to a renewable energy-supported society. Especially, the development of electric appliances and vehicles has been remarkable, because these are non-carbon consumers and are anticipated for an eco-friendly society. Batteries are the dominant electric energy-saving device and their development is encouraged as well as that of the electric generation devices like solar cells. Different from batteries possessing large electric storage ability, capacitors are characterized by rapid charge/discharge, high power density and long cycle ability based on the energy storage mechanism,[1] and research on supercapacitors is focused to increase electric storage efficiency.

Graphene is a type of carbon materials and possesses novel physicochemical properties[2] and it is a promising candidate for broad applications.[3] It is also a representative material for electric double layer capacitors (EDLC). The adequate doping of heteroatoms including nitrogen and boron on EDLCs can tailor the electronic properties of graphene and improve the efficiency of the specific capacitance.[4] However, the capacitance of EDLCs is not large, although the stability is sufficiently high.[5] On the other hand, pseudocapacitors, materials which are conductive polymers and metal oxides, give rise to large capacitance but less stability.[5] Thus, a hybrid supercapacitor of EDLC and pseudocapacitor is preferable because of the complementarity.[6–9] For instance, a hybrid supercapa-

citor of carbon nanohorn (CNH) and polyaniline presented synergetic capacitance increase while maintaining the stability of an electrode.[6] Otherwise, the addition of metal oxide on an EDLC material encourages the capacitance efficiency of an electrode.[7]

Transition metal hydroxides/oxides, for instance, Co_3O_4,[5] NiO,[10,11] MnO_2, V_2O_5, Fe_3O_4,[12] Fe_2O_3,[3] $Ni(OH)_2$,[11] $Co(OH)_2$, which are typical pseudocapacitor materials, have been investigated due to their abundance,[13] high theoretical specific capacitance,[14] low cost,[1] harmlessness, and faradic reaction to store energy. Although their lower accessible surface area,[13] relatively poor electrical conductivity, and poor reversibility[5] have limited their potential application in energy storage devices, the addition of them on EDLC may encourage the capacitance efficiency of an electrode.[6–8]

Another novel strategy proposed to enhance the performance of supercapacitor is the application of the external magnetic field during electrochemical measurement on the electrochemical cells consisting of magnetic material electrodes.[7] The magnetic field induced in the magnetic material using the external magnetic field may play a fundamental role in the electrochemical charging/discharging process and the velocity of ions/charges. The presence of the external field strongly will affect the transportation of charge carriers, improve the effective resistance and enhance the capacitive behavior of the magnetic electroactive electrode materials.

In this work, we synthesized nitrogen-, boron- and boron/nitrogen-doped graphenes (NG, BGO, and BNG) and investigated their electrochemical behavior. In addition, CNH was also treated with nitrogen to dope it for comparison with NG. Graphene and CNH are both allotropes of carbon materials but the former is a two-dimensional graphitic sheet and the latter consists of horn-like units of graphitic structure and takes the particle size of 80–100 nm.[15] This morphological difference should diversely affect electrochemical properties. In addition, different types of magnetic metal oxides were conjugated with NG and the electrochemical behaviours under an external magnetic field were compared among magnetic metal oxide species. Since metal oxide is in a category of pseudocapacitor material, the hybrid with carbon material will be expected to keep the advantage of high capacitance and long cycle life, and such behaviours including under an external magnetic field should depend on the metal species.

2. Experimental Section

Materials. Graphite flake (C > 99%) was provided by Ito graphene Co, Ltd., Japan. CNH and oxidized CNH was purchased from NEC, Japan. Potassium permanganate (98%), aqueous hydrogen peroxide (35 wt%) solution, urea (99.5%), N-methyl pyrrolidone, Iron(III) chloride hexahydrate (99%), cobalt(II) nitrate hexahydrate (99%), and boric acid (99.5%) were obtained from Acros Organics, UK. Carbon black (99.9+%), iron(II) chloride tetrahydrate and nickel(II) nitrate hexahydrate (99%) were purchased from Alfa Aesar, USA. Nafion® (perfluorinated resin) solution (5 wt% in lower aliphatic alcohols and water, contains 15–20% water) and polyvinylidene fluoride were purchased from Sigma-Aldrich, USA. Indium tin oxide (ITO) glass was purchased from AimCore Technology, Taiwan. Other reagents were commercial grade.

Synthesis of Graphene Oxide (GO) and Nitrogen-, Boron- and Boron/Nitrogen–Doped Graphenes (NG, BGO, and BNG). GO sheets were synthesized from graphite flake by a modified Hummers method.[16–18] Briefly, graphite flake (0.5 g) was mixed with potassium nitrate (0.5 g) and potassium permanganate (1.5 g) in concentrated sulfuric acid (25 ml) under stirring in an ice bath. After the mixture reacted at 35 °C for 24 h under stirring, it was diluted with water; (20 ml) was poured slowly into the mixture in the ice bath and after 10 min, H_2O_2 (30%, 5 ml) was added into the reaction system. The product was purified by centrifuging with water and then dried overnight in a vacuum at 40 °C.

Aqueous GO dispersion (1 mg/ml, 40 ml) mixed with urea (mass ratio GO:urea = 1:300) was sonicated for 3 h and reacted in a Teflon-lined autoclave for 12 h at 180 °C. The product was purified by filtration and dried overnight at 60 °C. The product is NG, because the urea-treatment also reduced graphene oxide besides doping nitrogen. Reduced graphene (rG) was prepared using the same procedure without urea.

Boric acid (445 mg) was added to the homogenous aqueous GO dispersion (1.5 mg/ml, 60 ml) under vigorous stirring for 1 h, and the dispersion was incubated in a Teflon-lined autoclave at 180 °C for 12 h. The product (BGO) was purified the same as the purification of NG.[19]

Aqueous GO dispersion (1 mg/ml, 40 ml) mixed with urea and boric acid (mass ratio GO:urea:boric acid = 1:300:300) was sonicated for 3 h and incubated in a Teflon-lined autoclave at 180 °C for 12 h.[17,19] The product (BNG) was alike purified.

Synthesis of Acid-Treated Single-Wall Carbon Nanohorns (acid-CNH) and Nitrogen-Doped Carbon Nanohorns (N-CNH). Commercial oxidized-CNH (50 mg) mixed with HNO_3 (69%, 30 ml) was refluxed under stirring for 1 h. The product (acid-CNH) was filtered through a cellulose acetate membrane (pore size 0.2 μm), washed by filtration with water and dried overnight at 40 °C. N-CNH was obtained by urea-treating an aqueous acid-CNH dispersion and purifying by the same procedure as NG.[17]

In Situ Deposition of Magnetic Metal Oxides on NG. In situ deposition of magnetic metal oxides on NG was performed by the reduction of metal precursor adsorbed on NG.[20] An aqueous solution of metal precursor (cobalt(II) nitrate hexahydrate (90.75 mg), nickel(II) nitrate hexahydrate (291.99 mg), or a mixture of iron(II) chloride tetrahydrate (64.4 mg) and iron(III) chloride hexahydrate (175.14 mg) at a mole ratio of 1:2) was mixed with an aqueous dispersion of NG (2 mg/ml, 100 mg) and stirred for 1 h. After adding an aqueous ammonium solution, the mixture was stirred at 80 °C for 1 h. The product was separated with a magnet, washed with water, and dried at 50 °C for 12 h in a vacuum oven. The final products of Co_3O_4/NG and NiO/NG were collected by the calcination of hydrothermal products at 300 °C for 2 h. The composition of Fe_3O_4, Co_3O_4, and NiO obtained from calcination of final products at 800 °C for 2 h were 32, 19, and 36%, respectively.

Instruments. Characterization was performed on a transmission electron microscope (TEM, JEOL JSM-2000FX II, Japan), a Fourier transform infrared (FTIR) absorption spectrometer (Nicolet Thermos Scientific 6700, USA), and thermogravimetric analysis (TGA, TA Q500 appliance, USA) with a heating rate of 10 °C/min under N_2 gas flow at 40 ml/min and

air flow at 60 ml/min. Nitrogen adsorption-desorption isotherms were measured at −196 °C (77 K) on a BELSORP-max instrument, Japan. Before the adsorption measurements, the samples were preheated at 110 °C for 3 h under vacuum. The specific surface area was calculated based on the BET (Brunauer-Emmett-Teller) method, and the pore size distribution was obtained from the desorption isotherms using the Barrette-Joyner-Halenda (BJH) method. The X-ray photoelectron spectra (XPS) were recorded on a theta probe ESCA by VG Scientific ESCALAB 250 from UK. Powder X-ray diffractions (XRD, D2 PHASER X-ray diffractometer) were obtained using a Cu target ($\lambda = 0.154$ nm) at a scan rate of 0.1°min^{-1}. An electrochemical workstation (ZAHNER Messsysteme, model XPot, Germany) was used for electrochemical measurements.

Electrochemical Measurement. The preparation of the working electrode followed the Nafion binder method.[6] A sample suspension (15 mg/ml) in ethanol was sonicated for 2 h, mixed with Nafion (250 µl) and stirred for 2 h. The homogeneous mixture (100 µl) was spin-coated at a speed of 800 rpm for 10 s (step 1) and at 1300 rpm for 30 s (step 2) on an ITO-coated glass (1 × 2 cm^2 piece) precleaned with detergent, solvents, water and ultraviolet light irradiation, and the electrode was dried at 50 °C for 2 h. The electrodes of metal oxide-doped materials were fabricated by mixing them (85 wt%) with carbon black (5 wt%, carbon black to NG: 1:17 weight ratio) and a dispersion of polyvinylidene fluoride in N-methyl pyrrolidone (10 wt%), stirring overnight at 45 °C after sonication (Branson 1210 Ultrasonic Cleaner, Yamato, Japan) for 2 h, casting the slurry (20 µl) on pre-cleaned ITO-glass substrate (1 cm × 1 cm) and drying.[21]

Electrochemical measurements were carried out in a 1 M NaCl electrolyte solution using three-electrodes of a working electrode prepared above, an Ag/AgCl (3 M KCl) reference electrode and a Pt wire counter electrode. All measurements were carried out at room temperature. The cyclic voltammetry (CV) was scanned from 5 to 100 mV/s scan rates, the galvanostatic charge/discharge (GCD) was measured at current densities ranging from 0.8 to 4 A/g, and the electrochemical impedance spectroscopy (EIS) was measured in a frequency range of 100 mHz to 100 KHz.

To examine the effect of the external magnetic field, a homogeneous magnetic field was applied in an electrochemical cell set at the inflection point of a Helmholtz coil (PASCO EM-6723 Field Coils, KYS Tech. Co. Ltd., Taiwan) connected to the DC power supply.

Specific capacitance Cs [Fg^{-1}] was calculated from eq (1):[6,7,22]

$$\mathrm{Cs} = \int \frac{I}{m} dV / \nu \Delta V \tag{1}$$

where I [A] is the current, m [g] is the mass of active material, V [V] is the potential, ΔV [V] is the potential window and ν [Vs^{-1}] is the scan rate.

For the electrochemical measurements under the external magnetic field, the electrochemical cell was kept at the inflection point between two Helmholtz coils of radius a (= 0.1 m) with N (= 500) turns of wire supplying the electric current I (= 2 A) from a DC power supply (Scheme 1). The applied field at the centre was fixed orthogonal to the unit normal to the electrode surface. Applying eq (2),[23] the calculated magnetic field $\boldsymbol{B}$ at the centre was 8.98 mT.

$$\boldsymbol{B} = \mu_0 NI/a(1 + (x/a)^2)^{3/2} \tag{2}$$

where μ_0 is the permeability constant (= 1.257 10^{-6} T·mA^{-1}), and x (= 0.05 m) is the radius of the coils, that is, the coil distance on axis to the inflection point.

3. Results and Discussion

Characterization of Materials. To identify the graphene with doped elements of nitrogen and boron, FTIR absorption spectra were measured and compared with those of GO and reduced GO in Figure 1A. In the spectrum of GO, the bands at 3396, 1727 and 1253 cm^{-1} can be assigned to the stretching vibrations of OH, C=O and C–O, respectively. However, because bands at 1624 and 1427 cm^{-1} assigned to antisymmetric and symmetric stretching COO^- vibration modes were also observed, carboxylic acid and carboxylate species coexist in GO. The C=C and C-C stretching vibration modes of the graphitic unit were observed at 1624 and 1123 cm^{-1}, respectively, although the former overlapped the COO^- vibration mode. In addition, phenolic OH and epoxide C-O-C vibration modes were assigned to bands at 1253 and 1123 cm^{-1}.[24] In the spectrum of reduced GO (rG), only the stretching vibration bands of C=C and C-C located at 1529 and 1120 cm^{-1} were observed, indicating the successful reduction of GO.

In the spectra of nitrogen-doped graphene, NG, CH and CH_2 stretching vibration bands appeared at 2920 and 2850 cm^{-1} respectively, but the C=O stretching band at 1727 cm^{-1} disappeared because the oxygen functional groups were reduced. Alternatively, besides graphitic C=C and C-C bands, a new band appeared at 1403 cm^{-1}, because N-doping produced the pyrrolic-NH or pyridinic-N structure (Scheme 2).[25] Additionally, the C-O-C and C-O stretching mode become the C-N/C-C stretching mode.[25–27] The C=O stretching band of boron-doped graphene, BGO, remains because the boron-doping reaction does not cause the reduction of oxidized groups[26] and the band located at 1205 cm^{-1} may be the C-B/C-C stretching mode. The IR spectrum of nitrogen/boron-doped graphene oxide, BNG, is similar to that of NG, indicating the majority of the doping is nitrogen.

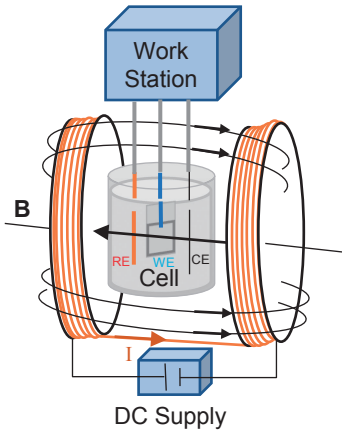

Scheme 1. Schematic illustration of an electrochemical cell equipped Helmholtz coil.

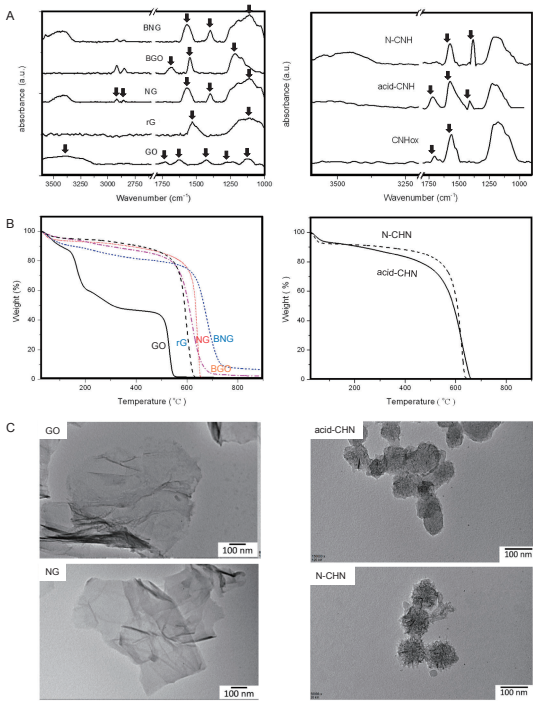

Figure 1. (A) FTIR spectra of GO, rG, NG, BGO, BNG, CNHox, acid-CNH and N-CNH. (B) TGA curves of GO, rG, NG, BGO, BNG, acid-CNH and N-CNH. (C) TEM images of GO, NG, acid-CNH and N-CNH.

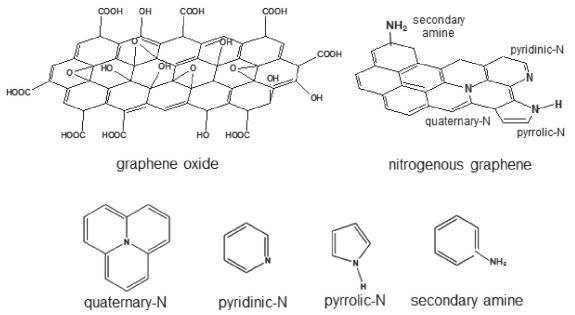

Scheme 2. Chemical structures of graphene oxide, nitrogenous graphene and nitrogenous moieties.

The FTIR spectra of commercial oxidized-CNH (CNHox), acid-CNH and N-CNH are shown in Figure 1A. Oxidized-CNH displayed bands at 1705 and 1560 cm^{-1}, which can be assigned to the C=O and C=C stretching vibration modes, respectively. The bands at 1250–1050 cm^{-1} are the overlapping of bands from graphitic C-C, epoxide, and phenol moieties. After the acid-treatment, a band at 1399 cm^{-1} appeared and bands at 1705 and 1559 cm^{-1} were intensified, indicating the appearance of carboxylate/carboxylic acid.

After the nitrogen-doping and concurrent reduction processes, N-CNH showed the disappearance of the bands at 1705 and 1399 cm^{-1} due to the loss of carboxylate/carboxylic acid moieties. Alternatively, an N-H bending vibration band from C-NH_2 or pyridinic-NH moieties appeared at 1385 cm^{-1}.[25] Because the intensity ratio of N-H/C=C on N-CNH is higher than that of NG (Figure 1A), the nitrogen-doping in N-CNH is more dominant than in NG. In addition, a band at 1576 cm^{-1} for C=C vibration mode may be overlapped by a C-N=C vibration mode from pyridinic moiety in N-CNH.[25,27]

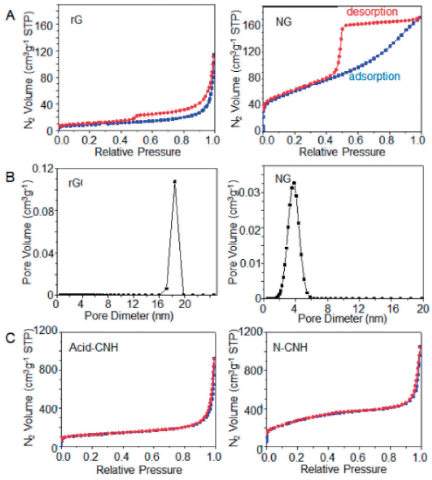

Figure 2. (A) Nitrogen absorption-desorption isotherms and (B) pore-size distributions of rG and NG, (C) nitrogen absorption-desorption isotherms of acid-CNH and N-CNH.

The thermal behaviours of GO, rG, NG, BGO and BNG were investigated by TGA. The weight loss from 25 to 150 °C is due to the existence of water and other volatile molecules. GO decomposed at the three steps from 150 to 550 °C (Figure 1B). The earlier two steps are mainly attributed to the decomposition of oxidized groups. The remaining weight loss was the decomposition of graphitic structure.[28] The TGA curves of rG, NG, BGO, and BNG showed a slight weight decrease (10–20 wt%) by 600 °C because of the decomposition of the remaining oxidized moieties.[29] The decomposition of the graphitic structure occurred at midpoints of 596, 623, 639 and 678 °C for rG, BGO, NG and BNG, respectively (Figure 1B). The TGA curves in Figure 1B also showed that BGO and BNG left residues of 2.01 and 6.5 wt%, respectively, which are the amounts of contained boron.[30]

The TGA curves of acid-CNH and N-CNH in Figure 1B show the simple thermal decomposition profiles. Initially, both TGA curves displayed the weight loss at temperature below 100 °C due to the removal of water and volatile molecules, and the graphitic structure decomposed above 600 °C with a midpoint of the decomposition at 619 °C. This value was lower than NG, indicating the easier decomposition of N-CNH, although acid-CNH was more stable than GO.

In the TEM images in Figure 1C, GO displayed sheet-like morphology and similar morphology was observed even for NG. Similarly, spherical structure with horns of acid-CNH was maintained even for N-CNH. These results indicate that the nitrogen-doping does not influence the morphologies of graphene and CNH.

For the assessment of surface characteristics, the specific surface area, pore size and pore volume of rG, NG, acid-CNH, and N-CNH were evaluated from the analysis of N_2 adsorption-desorption isotherms as shown in Figure 2. The rG and NG exhibited the characteristic hysteresis loop at relative pressures from 0.42 to 1 between the adsorption and desorption branches, indicating that the isotherms of rG and NG belong to the type IV (hysteresis type) for mesoporous materials.[27,31] The

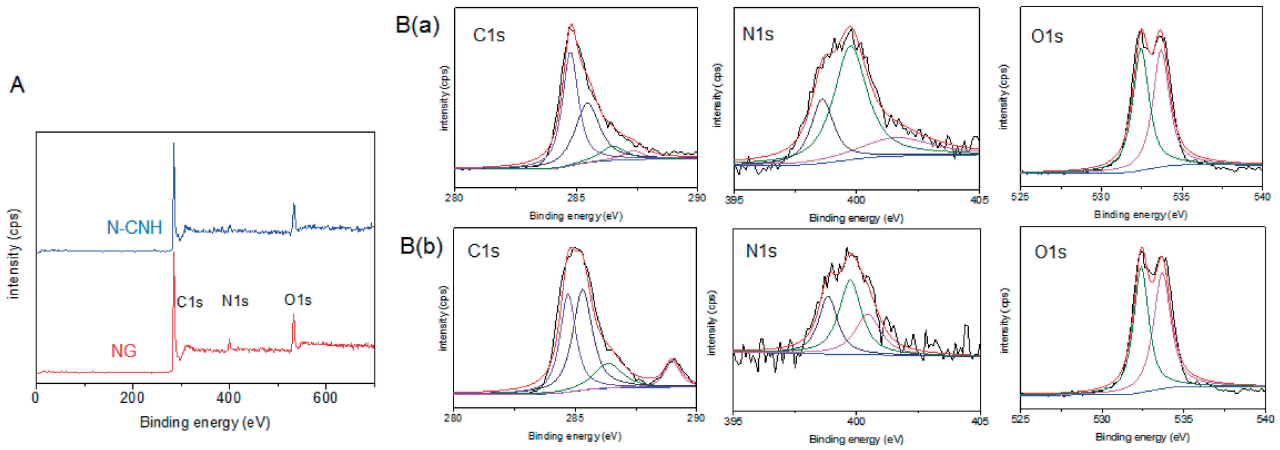

Figure 3. (A) XPS spectra of NG and N-CNH, (B) C 1s, N 1s, and O 1s of (a) NG and (b) N-CNH.

specific surface area of rG and NG were 30.4 and 218.6 m^2g^{-1}, respectively, and their pore size distribution in Figure 2B displayed a unimodal peak centred at 18.4 and 3.8 nm and the pore volume of 0.16 and 0.26 cm^3g^{-1}, respectively. This large increase in surface area and the decrease of pore size in NG indicates the strong influence of N-doping on the surface modification. On the other hand, acid-CNH and N-CNH displayed the type II isotherm (BET type) for non-porous materials (Figure 2C), and their specific surface areas were 419.6 and 977.8 m^2g^{-1}, respectively, which were higher than rG and NG due to the high acid-treatment and nitrogen-doping, because these procedures open the channels for nitrogen gas to load on the inner wall of horns.

The elemental compositions of NG and N-CNH were compared from XPS analysis. The XPS result in Figure 3A revealed the appearance of N1s peak besides C1s and O1s peaks in both NG and N-CNH, indicating that the nitrogen is successfully doped. The nitrogen content (9.03%) of NG was higher than that (2.43%) of N-CNH. Figure 3B displays the fine and deconvolution spectra of C1s, N1s and O1s peaks of NG and N-CNH.

The C1s spectrum of NG showed a main peak at 284.75 eV attributed to aromatic CC that is arranged in a conjugated honeycomb lattice. The peaks at 285.45 and 286.5 eV, respectively, may be attributed to CN (pyridine and pyrrole) originated from doped nitrogen. In the N1s spectrum, the main peak at 399.75 eV can be attributed to pyrrolic-N overlapped with C-NH_2, and pyridinic-N is located at 398.5 eV. The peak at 401.5 eV may be the binding energy of quaternary-N. The O1s spectrum showed two different peaks at 532.45 and 533.7 eV, which should be C=O and C-O bonds, respectively.[31] The above-mentioned results infer that the structural moieties of NG must be aromatic CC of graphitic structure and nitrogenated species (pyridine, pyrrole and quaternary nitrogen and secondary amine). However, C=O and C-O bonds were also observed, indicating the imperfect reduction in rG.

Figure 3 also shows the fine and deconvolution spectra of C1s, N1s and O1s of N-CNH. Although three C1s peaks at similar binding energies to these for NG were observed even for N-CNH, the fourth peak was observed at 289 eV in N-CNH, which is assigned to the C-NH_2 bond. Three peaks in the N1s spectrum and two peaks in the O1s spectrum of N-CNH were also observed as well as in NG. As a result, N-CNH also possessed graphitic CC, nitrogenated species (pyridine, pyrrole, quaternary nitrogen, and secondary amine) and CO bonds but the secondary amine in N-CNH is richer than in NG.

As estimated from the chemical structure of quaternary nitrogen, pyridine and pyrrole moieties, while quaternary nitrogen modifies the electronic structure of a graphitic structure, pyridinic-N donates one p-electron to the aromatic π system and has a lone electron pair[32] and pyrrolic-N contributes to the π system with one or two p-electrons.[33] Thus, these nitrogen-including moieties in NG and N-CNH will provide free valence electrons to interact with electrolyte and they may improve the electrochemical performance of graphene and CNH.

Characterization of Metal Oxide/Nitrogen-Doped Graphitic Compounds. Metal oxides of NiO, Co_3O_4 and Fe_3O_4 were deposited in situ on NG. Their particle sizes from TEM images (Figure 4A) were 58.8, 22.4, and 11.6 nm, respectively. Figure 4B shows the FT-IR spectra of NiO/NG, Co_3O_4/NG and Fe_3O_4/NG. These three IR spectra displayed a broad OH stretching vibration band at 3448 cm^{-1} of the remaining functional group in NG and no remarkable IR bands between 3000–800 cm^{-1}, because the characteristic bands of NG were weaker than the characteristic bands of metal oxides. The IR spectrum of NiO/NG indicated a Ni-O vibration band at 433 cm^{-1}. In the IR spectrum of Co_3O_4/NG, a band at 653 cm^{-1} is attributed to Co-O-Co stretching vibration mode and a band at 424 cm^{-1} are assigned to Co-O-Co deformation mode.[34] The characteristic Fe-O stretching vibration band of Fe_3O_4/NG was presented at 593 cm^{-1}.[35]

Figure 4C shows the structural information patterns of the powder X-ray diffraction (XRD) obtained for NG, NiO/NG, Co_3O_4/NG and Fe_3O_4/NG. The XRD patterns of NiO/NG, Co_3O_4/NG and Fe_3O_4/NG commonly display broad diffraction peaks at $2\theta = 25.3$–$25.6°$ (002) and 43.08° (400) deriving a graphitic structure of NG.[1,4] In addition, the diffraction peaks of Fe_3O_4/NG located at $2\theta = 30.56$, 35.91, 43.64, 56.93, and 62.69° can be indexed to (220), (311), (400), (511), and (440) planes of cubic Fe_3O_4 with a space group of Fd-3m (JPCPDF No. 65-3107). As seen in an XRD pattern of NiO/NG, the diffraction peaks at $2\theta = 37.4$, 43.7, and 62.9° can be assigned to (111), (200), and (220) crystal planes of cubic NiO[13] with a space group of Fm-3m (JPCPDF No. 47-1049). The diffraction peaks of Co_3O_4/NG at $2\theta = 19.04$, 31.5, 37.0, 44.0, 59.9, and

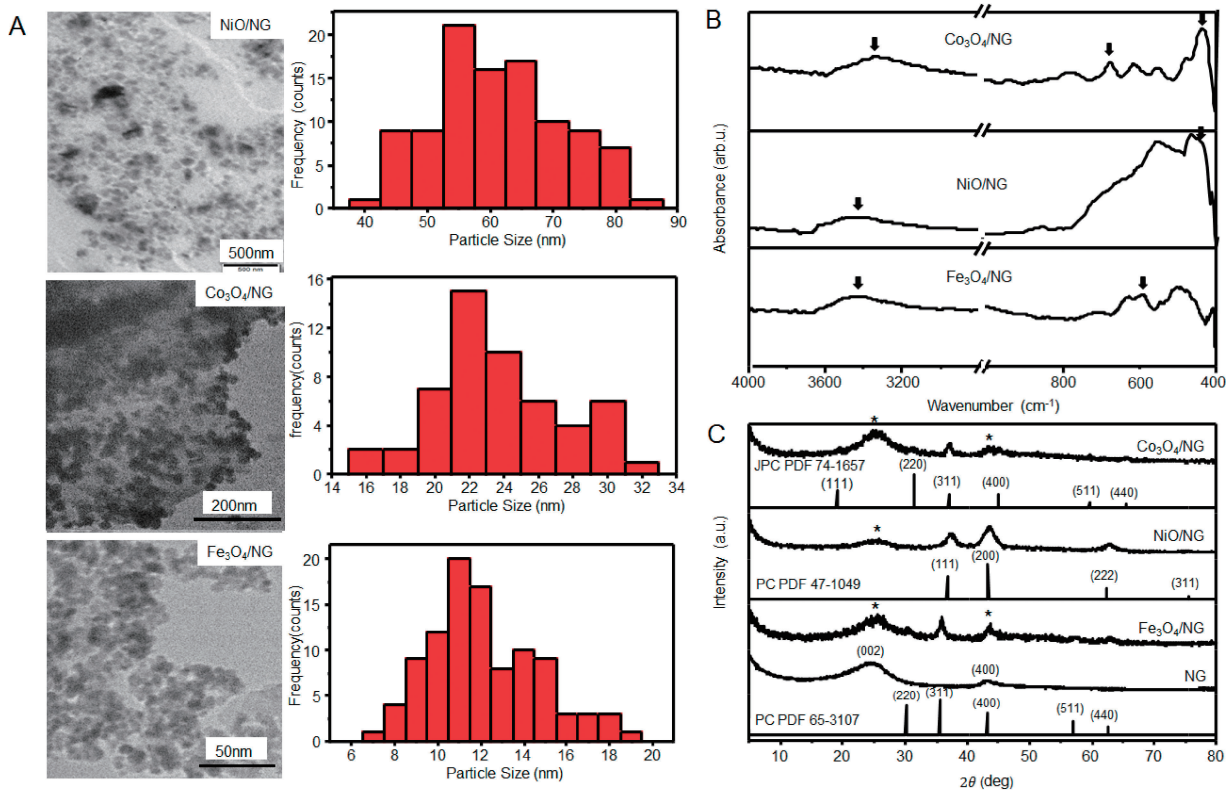

Figure 4. (A) TEM images and size distribution frequencies, (B) FTIR spectra and (C) XRD patterns of Co_3O_4/NG, NiO/NG, Fe_3O_4/NG and NG.

65.8° can be indexed to (111), (220), (311), (400), (511), and (440) planes of the cubic Co_3O_4 crystal[36] (a space group of Fd-3m (JPCPDF No. 74-1657)). Thus, the XRD results indicate that NG coexists with magnetic metal oxides.

Crystalline size can be calculated based on the Debye-Scherrer's equation.[37] When Bragg peaks of (111), (311) and (311) for NiO, Co_3O_4 and Fe_3O_4, respectively, are selected, the crystal sizes were calculated as 6, 16, 11 nm, respectively. While the sizes of Co_3O_4 and Fe_3O_4 were consistent with values from TEM images, the size of NiO from TEM was one order larger than that from XRD. This result may indicate that NiO nanoparticles on NG are secondary-aggregated particles.

Electrochemical Properties of Nitrogen, Boron and Nitrogen/Boron-Doped Graphene and Nitrogen-Doped Carbon Nanohorn. The carbon materials, which are EDLC materials, are conductive but normally they have rather low capacitance.[6–8] One of the possibilities for improving such character is the doping of additives in the carbon materials such as nitrogen, boron and so on.[4] The CV performance of NG, BGO, and BNG in 1 M sodium chloride was examined and compared with that of GO as shown in Figure 5A. The CV profile presented basically the rectangular-like shape characteristic to EDLC but displayed humps on the BG electrodes, indicating the contribution of the redox reaction on the surface of the electrode. Figure 5A also displays CV curves of acid-CNH and N-CNH with the rather typical EDLC profile.

Calculated specific capacitance was plotted in Figure 5B as a function of scan rate from 5 to 100 mVs^{-1}. The capacitance of GO, NG, BGO and NBG were 153, 303, 225 and 262 Fg^{-1} at 5 mVs^{-1}, respectively, decreased with increasing scan rate and reached 56, 117, 48 and 101 Fg^{-1} at 100 mVs^{-1}, respectively. Thus, the nitrogen-doping in GO enhances the capacitance performance more than the boron-doping. In addition, Figure 5B showed that the capacitance of acid-CNH and N-CNH were 219 and 248 Fg^{-1} at 5 mVs^{-1} and 108 and 118 at 100 mVs^{-1}, respectively. The results indicate that the nitrogen-doping on acid-CNH generates a slight increase of the capacitance, but NG has still better performance than N-CNH.

The galvanostatic charge/discharge (GCD) behavior measured at different current densities from 0.8 to 4 Ag^{-1} is plotted in Figure 6A. The charge/discharge plots of NG and N-CNH slightly deviated from the isosceles triangle shape, but obviously, the discharge time of NG at the same current density was longer than that of N-CNH, indicating NG has better performance on the storage like the knowledge from CV analysis. The difference in the capacitance behavior between NG an N-CNH can be explained by the difference in the surface characteristics. Since NG is a mesoporous material and its surface area is larger than N-CNH (Figure 2C), the larger amount of electrolytes are trapped by the rapid access and the fast transport of electrolytes on the surface of NG due to the provision of a more favourable path for penetration and transportation of ions into electrodes. Thus, the porous materials with large surface area can improve the capacitance performance.[27,31]

The XPS result also displayed that the nitrogen content of NG is higher than N-CNH and the nitrogen element is incorporated as different N-containing moieties, such as pyridine, pyrrole, quaternary nitrogen and amine (Figure 3). The former

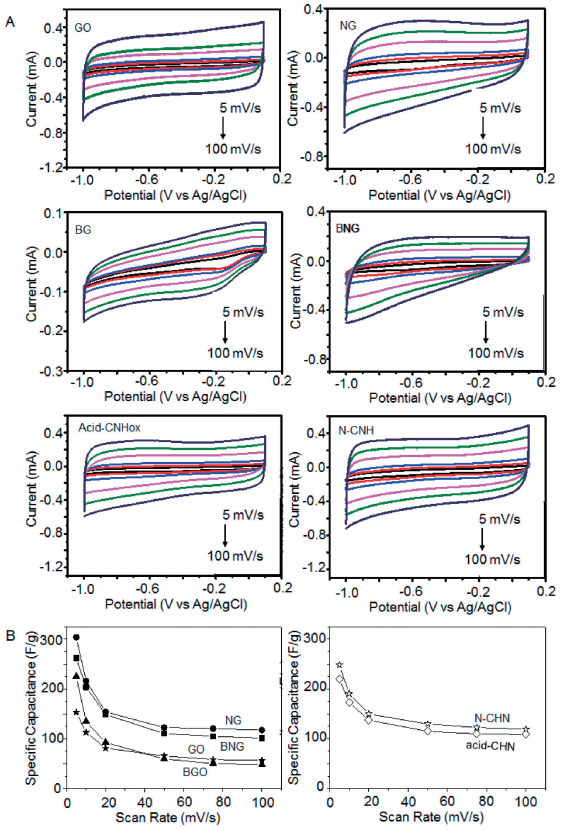

Figure 5. (A) Cyclic voltammograms at different scan rates from 5 to 100 mVs^{-1} and (B) specific capacitance as a function of scan rate of GO, NG, BGO, NBG, acid-CNH and N-CNH electrodes.

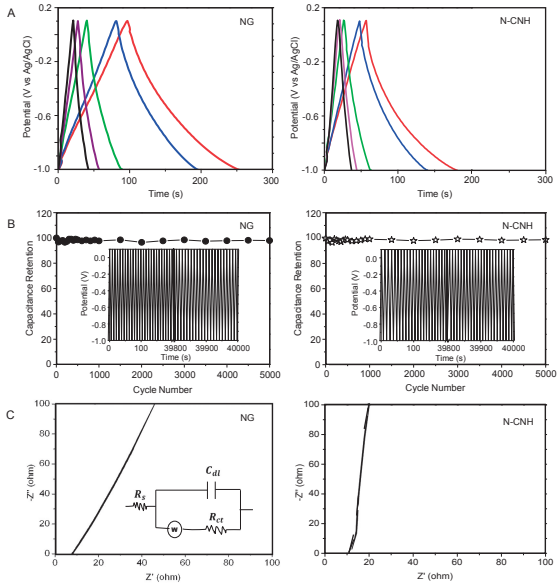

Figure 6. (A) GCD curves of NG and N-CNH electrodes at different current densities from 0.8 to 4 Ag^{-1}. (B) Cycle lives of capacitance retention of NG and N-CNH as a function of cycle number. Inset; charge-discharge curves of NG and N-CNH at the first 32 and the last 32 cycles. (C) Nyquist plots of NG and N-CNH electrodes at frequencies ranging from 100 mHz to 100 kHz. The inset indicates the equivalent electrical circuit.

three moieties can provide free valence electrons, which interact with electrolyte and enhance the performance on the capacitor.[17]

To compare the influence of nitrogen doping between different carbon materials, the cycle stability was also measured at a current density of 7 Ag^{-1}, as shown in Figure 6B. During increasing the cycle numbers to 5000 cycles, the capacitances of NG and N-CNH still retained 97.9% and 98.7% of their initial specific capacitance, respectively. The first 32 cycles and the last 32 cycles for NG and N-CNH are presented as an inset in Figure 6B. It was found that the shapes of the charge-discharge curves were nearly kept, indicating the good reversibility for both.

The electrode conductivity and ion-transport can be assessed by electrochemical impedance spectroscopy (EIS). The equivalent circuit (the Randles circuit model) includes the solution resistance (R_s, 100 Ω), the charge-transfer resistance (R_{ct}), the EDLC (C_{dll}, 10 μF) and Warburg diffusion impedance (W_d, 50 $\Omega s^{-0.5}$), as shown in the inset of Figure 6C. The Nyquist plot displayed the resistance values at $R_{ct} = 8.75$ and 10.03 Ω for NG and N-CNH, respectively. These results show that NG has a faster electron transfer ability than N-CNH, being consistent with the capacitance behaviour.

The doping of heteroatoms is an effective way to tailor the electronic, chemical, and physical properties of GO.[4] Among heteroatoms, nitrogen effectively configurates nitrogen-doped units (pyridine, pyrrole, quaternary nitrogen and secondary amine) in graphitic structure (see Scheme 2 and Figure 3) to obtain high surface area, attenuate pore size (Figure 2), and good electronic conductivity.[38] The nitrogenous moieties except amine can provide lone pair electrons, which interact with electrolytes and enhance the performance of the capacitor. The pyridinic-N and pyrrolic-N improve the redox reaction, and, meanwhile, the quaternary-N can enhance the electrical conductivity and hence facilitates electron transport during charge-discharge.[17] Since NG is a mesoporous material, the larger amount of electrolytes are trapped and the transport of electrolytes on the surface of NG becomes easier because NG provides a more favourable path for penetration and transportation of ions into electrodes.[17]

The surface area of CNH is more than 10 times and about 2 times larger than rG and NG, respectively, and that of N-CNH is double that of CNH (see Figure 5). However, the difference in capacitance is not so large (see Figure 5). Both rG and NG are porous materials, but CNH an N-CNH are nonporous, that is, there are no pores. Thus, a sufficient amount of electrolytes can adsorb on CNH and N-CNH, but they have only slightly the essential path to penetrate and transport ions to electrodes.[17] Accordingly, the porosity of the material is important for affecting its energy storage device application. Since the nitrogen content was also different between NG and N-CNH (9.03 and 2.43%, respectively, from XPS analysis), the low conductivity by less nitrogen doping may compensate for the high conductivity ability from the large surface area on CNH.

Electrochemical Properties of Magnetic Metal Oxide-Deposited Nitrogen-Doped Graphene under the External Magnetic Field. CV curves at different scan rates for metal

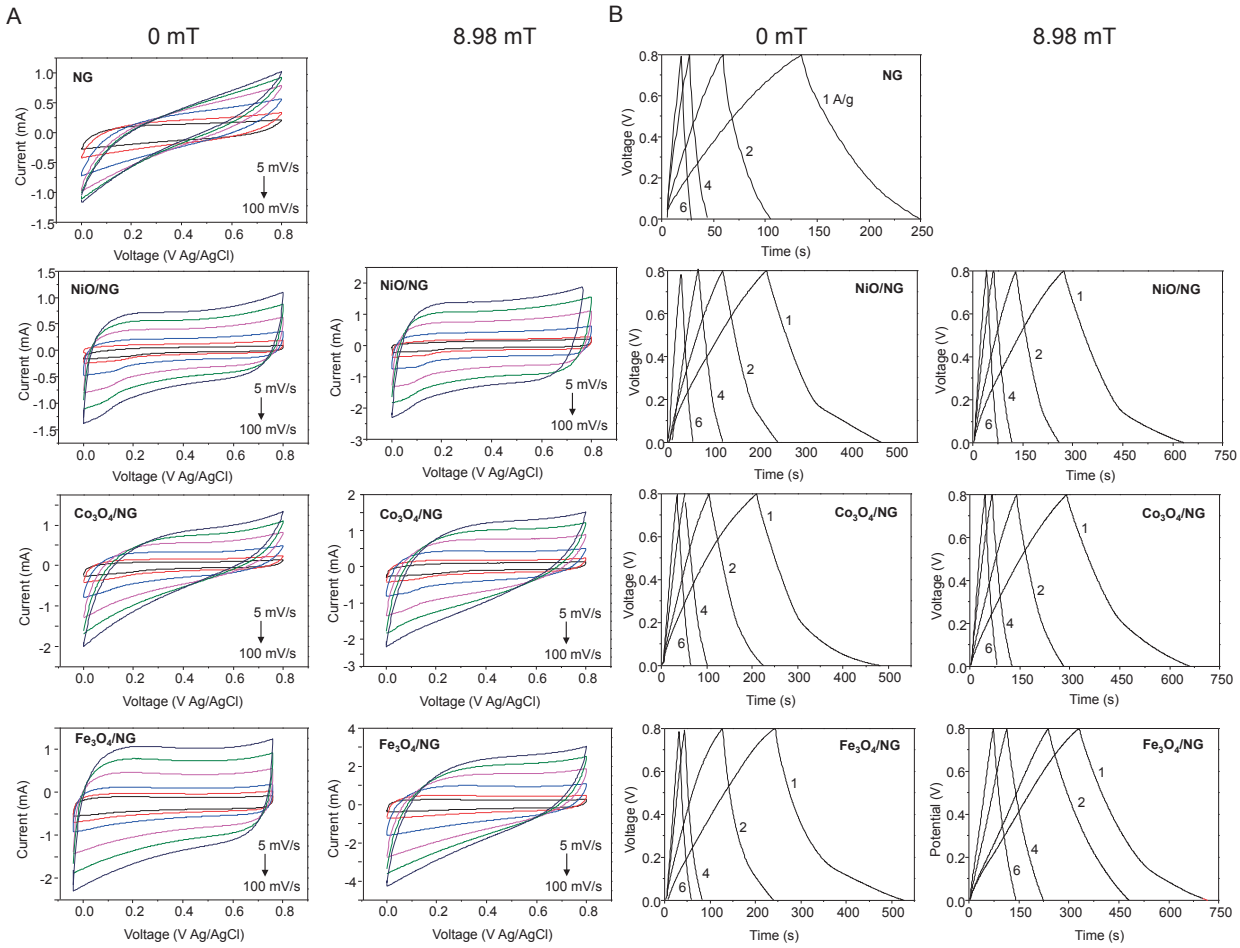

Figure 7. (A) CV curves at different scan rates and (B) charge-discharge plots at different current densities for NG and metal oxide/NG electrodes at 0 and 8.98 mT.

oxide/NG composites are plotted in Figure 7A and compared at the external magnetic field of 0 and 8.98 mT. Figure 8A collects specific capacitance vs scan rate at 0 and 8.98 MT. The CV curves of NG and metal oxide/NG composites took the EDLC capacitor profiles, and similar profiles were found even under the magnetic field, although the increases in the current density occurred under the application of the external magnetic field. The calculated specific capacitances, which always decrease with increasing scan rate, were heightened in the order of NG < NiO/NG < Co_3O_4/NG < Fe_3O_4/NG at the scan rate of 5 mVs^{-1} without/with magnetic field, as shown in Figure 7A. Such order follows even at a high scan rate up to 100 mV/s except the case of Fe_3O_4/NG at no magnetic field; it was lower than that of Co_3O_4/NG and close to NiO/NG.

The GCD measurements without/with external magnetic field were conducted with a potential range from 0 to 0.8 V at different current densities of 1, 2, 4, and 6 A/g and shown in Figure 7B. The current resistance drop did not appear in all GCD curves even under the magnetic field, while the discharging time was the highest for Fe_3O_4/NG under the magnetic field, consistent with the tendency of capacitance from the CV curve.

The Nyquist plots of EIS for NG and metal oxide/NG composites are displayed in Figure 8B and the numerical values of

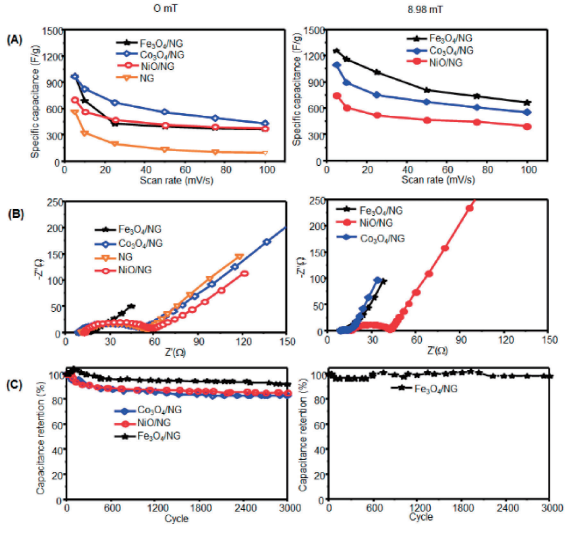

Figure 8. (A) Specific capacitance versus scan rate, (B) Nyquist plots of EIS, and (C) capacitance retention for 3000 cycles of NG and metal oxide/NG electrodes at 0 and 8.98 mT. Current density in (C); 10 A/g for 0 mT and 20 A/g for 8.98 mT.

Table 1. Specific capacitance, resistance, capacitance retention, BET surface area, total pore volume and mean pore diameter of NG and metal oxide/NG electrodes at 0 and 8.98 mT.

		NG	NiO/NG		Co_3O_4/NG		Fe_3O_4/NG	
Magnetic field (mT)		0	0	8.98	0	8.98	0	8.98
Scan rate (mV/s)	5	566	697	747	963	1092	973	1254
Specific capacitance (F/g)	100	95	370	394	432	553	363	657
Resistance (Ω)	Rs	10.95	14.95	12.35	8.72	8.68	8.78	8.64
	Rct	45.69	44.14	29.70	43.16	3.88	6.69	3.44
Capacitance retention (%)			85		83		92	98
BET surface area (m^2/g)		219	259		185		213	
Total pore volume (cm^3/g)		0.26	0.289		0.387		0.263	
Mean pore diameter (nm)		3.8	4.5		8.4		4.9	

resistances (Rs and Rct) are listed in Table 1 with the specific capacitance values at 5 and 100 mV/s scan rates. Both resistance values decreased under the external magnetic field at the inverse order of the capacitance. These results indicate that the specific capacitance enhancement is involved the fast contact and charge transferring process which are the inverse of the resistances.

The capacitance retention of metal oxide/NG composites was tested at 0 and 8.98 mT and shown in Figure 8C. The cyclic stability at 3000 cycles increased in the order of Co_3O_4/NG (83%), NiO/NG (85%) and Fe_3O_4/NG (92%) at 0 mT. Under the external magnetic field, the cycle stability at 3000 cycles on Fe_3O_4/NG was the highest (98%), indicating that the Fe_3O_4/NG composite surface was more accessible than without the external magnetic field. However, the stability fluctuated during the 3000 cycles, suggesting the instability of the charge transfer route under the magnet field.

The reported capacitance retention was 82–97% for NiO/NG electrode,[11] Co_3O_4/rGO,[36,39] and N-graphene/Fe_3O_4 nanocomposite electrodes.[35] These retention values are rather lower than those of supercapacitors of carbon materials and their composites with conductive polymers.[6] However, the retention values of magnetic material/carbon material composites are improved as well as the present report.[12,40]

Concerning the difference of specific capacitances of NG from Figure 5 and Figure 8 on the fabrication process of the former working electrode, Nafion was added as a binder, but Nafion was insufficient as a binder for a metal oxide/NG working electrode. Thus, a binder for metal oxide/NG was a mixture of carbon black and polyvinylidene fluoride and an NG electrode prepared from the same binder was also examined. Then an additive carbon black may act as a protector for hindering the restacking of graphene sheets which enhances the electrical conductivity,[38,41] indicating that the proper selection of the binder can play a role of binding the electroactive material and the conductive substrate. It has been reported that the result obtained using Nafion (10%) was less than that of polyvinylidene fluoride (5%) in the same electrode material.[42]

The complexation of metal oxides with NG improves the properties of carbon materials by mainly enhancing charge transportation and separation[2] and preventing nitrogen doped-graphene oxide from re-stacking and accessible area loss. Table 1 indicates that the charge transferring process is passive on NiO/NG and Co_3O_4/NG hybrid electrodes but it is approved on the Fe_3O_4/NG electrode. The order may originate

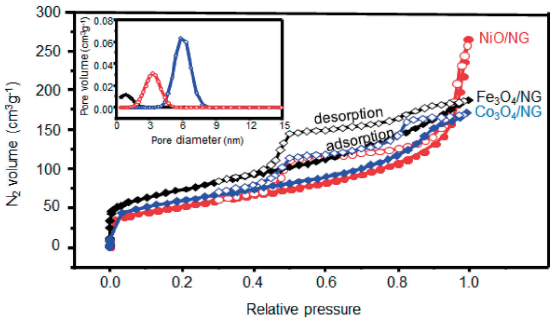

Figure 9. Nitrogen absorption-desorption isotherms of magnetic metal oxide/NG powders. Inset is the pore-size distributions.

from the electrical conductivity of the metal oxides. It increases in the order of NiO (~0.714 $(\Omega\cdot cm)^{-1}$) < Co_3O_4 (10^{-3}–10^3 $(\Omega\cdot cm)^{-1}$) < Fe_3O_4 (10^2–10^3 $(\Omega\cdot cm)^{-1}$).[43,44]

Nitrogen adsorption-desorption isotherms were measured for the magnetic metal oxides/NG powders. The BET nitrogen adsorption-desorption isotherms and the corresponding BJH pore size distribution plots are presented in Figure 9, and obtained numerical values are listed in Table 1. The isotherms of Co_3O_4/NG and Fe_3O_4/NG exhibited curves of type IV but that of NiO/NG was type II, although three isotherms revealed hysteresis which is ascribable to NG (see Figure 2A). As seen in Table 1, the characteristics of BET surface area and porosity can be mainly attributed to NG and, moreover, Fe_3O_4/NG is not the highest on surface area and porosity. Thus, the correlation of the specific capacitance to the surface area and porosity was not specified on metal oxide/NG hybrid materials.

On the other hand, the influence of particle size on the capacitance performance has been investigated for nickel oxide nanoparticles.[45,46] The capacitance increased with decreasing the particle size from 22 to 12 and 8 nm or from 41 to 21 and 6 nm because of the increase in number of active sites for a faradaic reaction[1] or the favorable ion transfer.[2] Thus, the decrease of particle size among NiO, Co_3O_4 and Fe_3O_4/NG should correlate to the efficiency on capacitance. In fact, the particle size of ZnO remarkably influenced the power conversion efficiency of dye-sensitized solar cells.[47]

Under the external magnetic field, the magnetic force orthogonal to the velocity of ions/charges and to the applied external magnetic field (**B**) causes the electrolyte ions to migrate to the electrode surface, convect the bulk electrolyte and minimize the

resistance of the electrolyte along with that of charge transfer resistance.[1] The convection enforces the ions to move into even the inaccessible area of the electrode surface and, moreover, may affect the electric conductivity as well as the dielectric constant of the electrolyte at the electrical double layer.[12] The magnetic particle placed in an external magnetic field is governed by the external magnetic field (**H**) and the induced magnetization field (**M**) given by $\boldsymbol{B} = \mu_0(\boldsymbol{H} + \boldsymbol{M})$, where μ_0 is the permeability of free space and is perpendicular to the Lorentz force and velocity of ions/charges in movement. The induced magnetization of the magnetic nanoparticles attached to the NG sheet affects the strength of the net magnetic field and hence the Lorentz force. Compared to the absence of the external magnetic field, the exposed electrochemical cell and electrode material to external magnetic field highly influence the velocity of ions/charges that reduces resistance, improve interface charge density, and enhance the supercapacitor performance using Lorentz force effect.

Supercapacitor investigations under magnetic field are very scarce. Zhu et al.[40] reported the capacitance enhancement induced by magnetic field at 720 Gauss on Fe_2O_3/graphene materials. Pal et al.[1] have investigated the effect of external magnetic field (0.125 T) on Fe_3O_4/reduced graphene oxide hybrid materials. However, they did not change the magnetic field intensity. According to our previous report,[7] the capacitance efficiency of electrode including magnetic metal oxides was encouraged by applying a magnetic field up to 1911 Gauss. Thus further experiments are expected to clarify the effect of magnetic field on supercapacitors.

4. Conclusions

In summary, when graphene oxide, a typical electric double layer capacitance material, is nitrogen-doped, its capacitance increases, because doped nitrogen provides lone pair electrons to interact with electrolyte.[48] Thus, the nitrogen-doping is effective to enhance the capacitance performance. However, since the capacitance of NG is still low, the hybridization with pseudocapacitor is promoted. Accordingly, hybrid materials of NG with metal oxides were prepared. Although NiO, Co_3O_4 and Fe_3O_4 are not popular as capacitance materials and their capacitance is not so large, the capacitance increased after being hybridized. Moreover, because the current metal oxides are magnetic materials, the hybrid electrodes display the enhanced performance of capacitors under external magnetic fields. Although the enhancement effect was different depending on the metal oxide species, such difference could be explained by the different electrical conductivity and by the Lorenz force. Although it can be demonstrated in the present situation, Fe_3O_4/NG has higher potential as a supercapacitor electrode under external magnetic field than NiO/NG and Co_3O_4/NG, the remaining issue is the fluctuation of capacitance retention of Fe_3O_4/NG electrode under external magnetic field. The extended current study should include other additive materials to compensate for the stability of the supercapacitor.

Electrical conductivity is an electric response and indicates the easiness of electrical conductance in a substance. Thus, this parameter is a typical barometer of electron transfer. Hence, it may play the role of electric sensor but if the electric current is weak, the issue should be its sensitivity and enhancement using external factors must be exercised. Magnetic fields are of unique character but a conventional additive force on the system. Thus, the report in this study will be extended as a highly sensitive electric sensor.

This investigation was partly supported by Ministry of Science and Technology, Taiwan (MOST 107-2221-E-001-067-). M.C.F. gratefully acknowledges National Taiwan University of Science and Technology, Taiwan, for financial support in the form of a PhD student scholarship.

References

1 S. Pal, S. Majumder, S. Dutta, S. Banerjee, B. Satpati, S. De, *J. Phys. D: Appl. Phys.* **2018**, *51*, 375501.
2 P. Majumder, K. Dutta, P. Dutta, *Int. J. Adv. Sci. Eng.* **2019**, *5*, 1032.
3 Z. Ma, X. Huang, S. Dou, J. Wu, S. Wang, *J. Phys. Chem. C* **2014**, *118*, 17231.
4 W. Fan, Y.-Y. Xia, W. W. Tjiu, P. K. Pallathadka, C. He, T. Liu, *J. Power Sources* **2013**, *243*, 973.
5 X. Yan, Y. Wang, Z. Ma, *Int. J. Electrochem. Sci.* **2018**, *13*, 1074.
6 C. C. Chang, T. Imae, *ACS Sustainable Chem. Eng.* **2018**, *6*, 5162.
7 M. M. Ahmed, T. Imae, *J. Magn. Magn. Mater.* **2019**, *491*, 165604.
8 M. M. M. Ahmed, T. Imae, *Phys. Chem. Chem. Phys.* **2016**, *18*, 10400.
9 M. Ujihara, M. M. M. Ahmed, T. Imae, Y. Yamauchi, *J. Mater. Chem. A* **2014**, *2*, 4244.
10 U. Patil, R. Salunkhe, K. Gurav, C. Lokhande, *Appl. Surf. Sci.* **2008**, *255*, 2603.
11 D. Pan, M. Zhang, Y. Wang, Z. Yan, J. Jing, J. Xie, *Chem. Phys. Lett.* **2017**, *685*, 457.
12 H. R. Naderi, P. Norouzi, M. R. Ganjali, H. Gholipour-Ranjbar, *Powder Technol.* **2016**, *302*, 298.
13 Q. Li, Q. Wei, L. Xie, C. Chen, C. Lu, F.-Y. Su, P. Zhou, *RSC Adv.* **2016**, *6*, 46548.
14 H. Chang, J. Kang, L. Chen, J. Wang, K. Ohmura, N. Chen, T. Fujita, H. Wu, M. Chen, *Nanoscale* **2014**, *6*, 5960.
15 B.-T. Zhang, X. Zheng, H.-F. Li, J.-M. Lin, *Anal. Chim. Acta* **2013**, *784*, 1.
16 Y. A. Workie, Sabrina, T. Imae, M. P. Krafft, *ACS Biomater. Sci. Eng.* **2019**, *5*, 2926.
17 L. Sun, L. Wang, C. Tian, T. Tan, Y. Xie, K. Shi, M. Li, H. Fu, *RSC Adv.* **2012**, *2*, 4498.
18 H. A. Becerril, J. Mao, Z. Liu, R. M. Stoltenberg, Z. Bao, Y. Chen, *ACS Nano* **2008**, *2*, 463.
19 Z. S. Wu, A. Winter, L. Chen, Y. Sun, A. Turchanin, X. Feng, K. Müllen, *Adv. Mater.* **2012**, *24*, 5130.
20 J. Cheng, X. Chen, J.-S. Wu, F. Liu, X. Zhang, V. P. Dravid, *CrystEngComm* **2012**, *14*, 6702.
21 M. M. M. Ahmed, T. Imae, J. P. Hill, Y. Yamauchi, K. Ariga, L. K. Shrestha, *Colloids Surf., A* **2018**, *538*, 127.
22 T. T. Debelo, M. Ujihara, *J. Electroanal. Chem.* **2020**, *859*, 113825.
23 H. Choi, J. Choi, G. Jang, J.-O. Park, S. Park, *Smart Mater. Struct.* **2009**, *18*, 055007.
24 Q. Hao, X. Xia, W. Lei, W. Wang, J. Qiu, *Carbon* **2015**, *81*, 552.
25 Y. Zhang, Z. Sun, H. Wang, Y. Wang, M. Liang, S. Xue,

RSC Adv. **2015**, *5*, 10430.
26 X. Mu, B. Yuan, X. Feng, S. Qiu, L. Song, Y. Hu, *RSC Adv.* **2016**, *6*, 105021.
27 A. Ariharan, B. Viswanathan, V. Nandhakumar, *Graphene* **2017**, *6*, 41.
28 S. Indrawirawan, H. Sun, X. Duan, S. Wang, *J. Mater. Chem. A* **2015**, *3*, 3432.
29 G. Xie, J. Cheng, Y. Li, P. Xi, F. Chen, H. Liu, F. Hou, Y. Shi, L. Huang, Z. Xu, *J. Mater. Chem.* **2012**, *22*, 9308.
30 A. Pullamsetty, R. Sundara, *J. Colloid Interface Sci.* **2016**, *479*, 260.
31 Z. Xing, Z. Ju, Y. Zhao, J. Wan, Y. Zhu, Y. Qiang, Y. Qian, *Sci. Rep.* **2016**, *6*, 26146.
32 G. Liu, X. Li, P. Ganesan, B. N. Popov, *Appl. Catal., B* **2009**, *93*, 156.
33 J. Li, Z. Ren, Y. Zhou, X. Wu, X. Xu, M. Qi, W. Li, J. Bai, L. Wang, *Carbon* **2013**, *62*, 330.
34 T. Ghorbani-Moghadam, A. Kompany, M. Bagheri-Mohagheghi, M. E. Abrishami, *J. Magn. Magn. Mater.* **2018**, *465*, 768.
35 L. Li, Y. Dou, L. Wang, M. Luo, J. Liang, *RSC Adv.* **2014**, *4*, 25658.
36 C. Sengottaiyan, R. Jayavel, P. Bairi, R. G. Shrestha, K. Ariga, L. K. Shrestha, *Bull. Chem. Soc. Jpn.* **2017**, *90*, 955.
37 T. A. Geleta, T. Imae, *Bull. Chem. Soc. Jpn.* **2020**, *93*, 611.
38 G. Rasines, P. Lavela, C. Macías, M. Zafra, J. Tirado, C. Ania, *Electrochim. Acta* **2015**, *170*, 154.
39 T. T. Nguyen, R. K. Deivasigamani, D. Kharismadewi, Y. Iwai, J.-J. Shim, *Solid State Sci.* **2016**, *53*, 71.
40 J. Zhu, M. Chen, H. Qu, Z. Luo, S. Wu, H. A. Colorado, S. Wei, Z. Guo, *Energy Environ. Sci.* **2013**, *6*, 194.
41 Y. Wang, J. Chen, J. Cao, Y. Liu, Y. Zhou, J.-H. Ouyang, D. Jia, *J. Power Sources* **2014**, *271*, 269.
42 Z. Zhu, S. Tang, J. Yuan, X. Qin, Y. Deng, R. Qu, G. M. Haarberg, *Int. J. Electrochem. Sci.* **2016**, *11*, 8270.
43 H. Sato, T. Minami, S. Takata, T. Yamada, *Thin Solid Films* **1993**, *236*, 27.
44 R. Drasovean, S. Condurache-Bota, N. Tigau, *J. Sci. Arts.* **2010**, *13*, 379.
45 N. Duraisamy, A. Numan, S. O. Fatin, K. Ramesh, S. Ramesh, *J. Colloid Interface Sci.* **2016**, *471*, 136.
46 S. P. Jahromi, A. Pandikumar, B. T. Goh, Y. S. Lim, W. J. Basirun, H. N. Limc, N. M. Huang, *RSC Adv.* **2015**, *5*, 14010.
47 M. T. Efa, T. Imae, *J. Taiwan Inst. Chem. Eng.* **2018**, *92*, 112.
48 Y. V. Kaneti, J. Zhang, Y.-B. He, Z. Wang, S. Tanaka, M. S. A. Hossain, Z.-Z. Pan, B. Xiang, Q.-H. Yang, Y. Yamauchi, *J. Mater. Chem. A* **2017**, *5*, 15356.

